GEOFLUIDS

Geofluids (2015) **15**, 577–591 doi: 10.1111/gfl.12128

The connectivity of pore space in mudstones: insights from high-pressure Wood's metal injection, BIB-SEM imaging, and mercury intrusion porosimetry

J. KLAVER[1], S. HEMES[1], M. HOUBEN[2], G. DESBOIS[1], Z. RADI[3] AND J. L. URAI[1]

[1]*Structural Geology, Tectonics and Geomechanics, Energy and Mineral Resources Group (EMR), RWTH Aachen University, Aachen, Germany;* [2]*Department of Earth Sciences, Utrecht University, Utrecht, The Netherlands;* [3]*Technoorg – Linda Ltd. Co., Budapest, Hungary*

ABSTRACT

Study of the pore space in mudstones by mercury intrusion porosimetry is a common but indirect technique and it is not clear which part of the pore space is actually filled with mercury. We studied samples from the Opalinus Clay, Boom Clay, Haynesville Shale, and Bossier Shale Formations using Wood's metal injection at 316 MPa, followed by novel ion beam polishing and high-resolution scanning electron microscopy. This method allowed us to analyze at high resolution which parts of a rock are intruded by the liquid alloy at mm to cm scale. Results from the Opalinus Clay and Haynesville Shale show Wood's Metal in cracks, but the majority of the pore space is not filled although mercury intrusion data suggests that this is the case. In the silt-rich Boom Clay sample, the majority of the pore space was filled Wood's metal, with unfilled islands of smaller pores. Bossier Shale shows heterogeneous impregnation with local filling of pores as small as 10 nm. We infer that mercury intrusion data from these samples is partly due to crack filling and compression of the sample. This compaction is caused by effective stress developed by mercury pressure and capillary resistance; it can close small pore throats, prevent injection of the liquid metal, and indicate an apparent porosity. Our results suggest that many published MIP data on mudstones could contain serious artifacts and reliable metal intrusion porosimetry requires a demonstration that the metal has entered the pores, for example by Wood's metal injection, broad ion beam polishing, and scanning electron microscopy.

Key words: BIB-SEM, Boom Clay, Bossier Shale, Haynesville Shale, mercury intrusion porosimetry, mudstones, Opalinus Clay, Wood's metal injection

Received 28 April 2014; accepted 12 January 2015

Corresponding author: Jop Klaver, Structural Geology, Tectonics and Geomechanics, Energy and Mineral Resources Group (EMR), RWTH Aachen University, Aachen, Germany.
Email: j.klaver@ged.rwth-aachen.de. Tel: +49 (241) 80-98445. Fax: +49 (241) 80-92358.

Geofluids (2015) **15**, 577–591

INTRODUCTION

Porosity and permeability analyses are of great importance in many fields of geosciences. These analyses are difficult in fine-grained rocks like mudstones. One of the common techniques used to measure porosity, pore-size distribution, and capillary breakthrough pressure in these rocks is mercury intrusion porosimetry (MIP) (e.g., Yang & Aplin 2007; Urai *et al.* 2008; Chalmers *et al.* 2012; Emmanuel & Day-Stirrat 2012; Josh *et al.* 2012; Busch & Amann-Hildenbrand 2013; Clarkson *et al.* 2013). MIP measures the volume of mercury injected into a pressure vessel containing the sample, at increasing pressures. Results of these measurements are traditionally interpreted as progressive entry of the mercury into the connected pore space of the rock. Pore-size distributions are calculated using Washburn's equation (Washburn 1921); more details of the morphology and connectivity of the pore space can be derived from the volume changes during lowering the mercury pressure (Webb 2001). However, a number of publications have shown that for various fine-grained materials such as cements, ceramics, and mudstones, the pore-size distributions obtained by MIP overestimate the small pores and underestimate the large pores because of complicated (e.g., ink-bottle) pore shapes (Abell *et al.* 1999; Diamond 2000; Hildenbrand & Urai 2003; Holzer *et al.* 2004).

The volume of injected mercury is interpreted as the total connected porosity and studies found correlations of MIP porosity in fine-grained rocks with other techniques. For example, a positive correlation was found between N_2 BET surface area and MIP porosity in shale gas reservoirs (Ross & Bustin 2009). Armitage *et al.* (2010) reported a clear positive relationship between the calculated porosity fractions using QEMSCAN® and MIP porosity in fine-grained rocks, although the MIP porosities are higher. Other studies that compared MIP with visible porosities obtained by broad ion beam and scanning electron microscopy (BIB-SEM) of fine-grained rocks also reported that the MIP porosities are larger (Klaver *et al.* 2012; Hemes *et al.* 2013; Houben *et al.* 2013). This discrepancy is mostly attributed to resolution issues, though there might be other reasons that could account for this gap. Due to the high pressures during MIP, deformation and compaction can occur, especially in mudrocks (Hildenbrand & Urai 2003) or coals (Yao & Liu 2012); however, this is traditionally interpreted as filling of the pore space. Compaction during MIP can account for a volumetric strain over 20% in kaolin clay (Penumadu & Dean 2000). In anisotropic rocks, this can be enhanced by the omnidirectional intrusion of the nonwetting fluid (Hildenbrand & Urai 2003). Moreover, a part of the intruded mercury may be due to filling of cracks caused by the sample preparation and dehydration (Klaver *et al.* 2012). Usually, the mercury intrusion volumes at low pressures (corresponding to large pores) in fine-grained rocks are the result of those cracks and are therefore removed from the analyses. It is unknown to what extent these cracks play a role at higher pressures, whether they get wider or close during intrusion and this cannot be deduced from MIP data alone. Until now, only limited direct observations exist on mercury-filled pore space (Moro & Böhni 2002; Giesche 2006) and there is no visible evidence whether mercury penetrates the small pores in fine-grained anisotropic rocks. The high injection pressures applied during MIP ($P_{injection} = P_{pore} = P_{confining} > 400$ MPa), the bottle-neck pore shape, and the anisotropic microstructure of the material can cause an effective stress (σ' - Terzaghi 1925) and compression of the rock instead of filling of the pore space, which cannot be distinguished based on the MIP data only. Recent advances in ion polishing have improved the imaging of pores in fine-grained rocks using BIB-SEM (e.g., Klaver *et al.* 2012; Hemes *et al.* 2013; Houben *et al.* 2013) and in 3D focused ion beam (FIB)-SEM image stacks (e.g., Holzer *et al.* 2004; Curtis *et al.* 2010; Keller *et al.* 2011). However, FIB-SEM tomography in fine-grained rocks often does not resolve the connecting pore throats (e.g., Houben 2013; Keller *et al.* 2013b; Houben *et al.* 2014b) and studied sample volumes are generally smaller than the representative volume element of heterogeneous mudstones (Keller *et al.* 2013a). By combining BIB-SEM with Wood's metal injection (WMI), the connected pore space can be visualized over representative areas and at high, nanometer-scale resolution. The advantage of Wood's metal (WM; 50% bismuth (Bi), 25% lead (Pb), 12.5% tin (Sn), 12.5% cadmium (Cd)) is that in the molten state, it has similar physical properties to mercury, but it melts at 70°C. This allows injection of the liquid WM into the pore space in a pressure vessel at 90°C, solidifying under pressure, and imaging the metal in the pores with BIB-SEM to obtain direct evidence of pores filled with the metal and compare it with MIP. In previous studies, WMI was used on a wide variety of materials, for example sandstone (Dullien 1981; Yadav *et al.* 1987), cements (Willis *et al.* 1998; Abell *et al.* 1999), induced fractures in concrete (Nemati 2000), feldspars (Dultz *et al.* 2006), salt and clays (Hildenbrand & Urai 2003), porous ash (Lloyd *et al.* 2009), porous carbonates (Galaup *et al.* 2012), Berea sandstone, and metagraywacke (Hu *et al.* 2012). These studies used lower pressures than MIP and used mechanical polishing which hinders accurate SEM imaging of nanopores (Klaver *et al.* 2012). Houben (2013) applied WMI on Opalinus Clay at pressures up to 200 MPa and found WM mostly in the cracks and large pores adjacent to the cracks, but not in matrix pores. Hu *et al.* (2014) injected a Barnet shale sample with liquid WM at 600 MPa and found no noticeable connected matrix porosity.

In this study, we aim to solve a series of research questions: (i) Where and how does the molten metal intrudes in heterogeneous mudstones?; (ii) Can we link the WMI-BIB-SEM observations to MIP bulk measurements?; and (iii) What is the effect of ion beam milling on the WM? We present results of high-pressure WMI experiments on four different fine-grained samples, in combination with cool BIB polishing and SEM imaging. Using high injection pressures equivalent to 3–5 nm in pore throat diameter, we show that the WM can fill accessible pores of at least 10 nm in size. To get a better understanding of the breakthrough pressure and possible artifacts during MIP, we also performed MIP on the samples and compared this with the WMI-BIB-SEM observations. The novelties of this research are the high injection pressures used for the WMI, and the subsequent (cool) BIB milling and SEM imaging.

SAMPLES AND METHODS

Sample description

Four fine-grained rock samples comprising various ranges of mineralogy and microstructure were investigated in this study (Table 1). Two samples, the Opalinus Clay, from the Mont Terri underground laboratory in Switzerland, and Boom Clay, from Belgium, are potential host rocks for the disposal of radioactive waste in Europe.

Table 1 Sample properties of all four samples. Abbreviations of the sample names are given in the second-column XRD obtained mineralogies are from previous studies, as well as the BIB-SEM porosities (see the references for more detailed information). BIB-SEM porosities depend on the magnification used, given in kx =1000 times between the brackets.

Sample	Abr.	Current depth [m]	QRTZ + FS [%]	Carbonates [%]	Clay [%]	BIB-SEM porosity [%]
Opalinus Clay (shaley facies)	OC	~300*	20	22	58	~2 (20kx)†
Boom Clay (EZE64)	BC	253	71	0	29	21 (30kx)‡
Haynesville Shale (SOM 4-4)	HS	4041	40	32	28	1.6 (20kx)§
Bossier Shale (SMY 4-2)	BS	3762	11	79	10	0.5 (20kx)§

*Thury & Bossart (1999).†Houben (2013).‡Hemes *et al.* (2013).§Klaver *et al.* (2015).

The Opalinus Clay is a Jurassic mudstone from the Dogger section with three different facies deposited in a marine environment during the Aalenian (Thury & Bossart 1999). For this study, we used a sample of the fine-grained, matrix-supported, and homogeneous shaley facies which consists of porous clay matrix (80%), fossil shells, pyrite framboids, and siderite and nonporous quartz, calcite, mica, and organic matter (Houben 2013). The microstructure and pore morphology of the shaley facies of the Opalinus Clay is well known from the work of Houben (2013), Houben *et al.* (2013, 2014a,b) and Keller *et al.* (2011, 2013a,b). Houben *et al.* (2013) classified different pore types and identified cracks down to 2 μm in width that accounted for 20% of the BIB-SEM porosity. The pore types consist of elongated pores mainly aligned to the bedding in the clay matrix (accounting for 50% of the porosity); randomly orientated angular pores (average pore diameter of 90 nm) in the fossils (accounting for 27% of the porosity); intercrystalline angular pores in pyrite framboids; intragranular elongated to roughly circular pores in siderite with jagged edges (Houben *et al.* 2013).

The Boom Clay Formation is a fine-grained marine sediment from the Rupelian. The sample investigated in this study (EZE64; ON-Mol-1-196; Zeelmaekers 2011; Hemes *et al.* 2013) originates from the Mol-1 borehole at the Mol-Dessel research site for radioactive waste disposal in Belgium from a level of depth of approximately 196 meters (bsl). The sample is from a silt-rich bed within the coarse-grained Belsele-Waas member, at the base of the Boom Clay Formation (Zeelmaekers 2011). The Boom Clay shows a very homogeneous mineralogical composition, with only quantify variations in the amount of different mineral phases (ONDRAF/NIRAS 2001). The clay fraction consists mainly of Illite and Kaolinite, with minor constituents of chlorite and smectite (Vandenberghe 1978a,b). The relative amounts of the different clay minerals to each other vary, as does the overall sum of clay minerals (between 30 and 70 Vol.-% with an average of 55%; ONDRAF/NIRAS 2001). The sample analyzed in this study contains approximately 72 dry wt.-% nonclay minerals and only about 28 dry wt.-% of clay. The median grain diameter of the sample is approximately 15.6 μm, but the sample contains a significant amount of silt and even fine sand-sized particles (>63 μm grain diameter). The microstructure of this sample consists mostly of silt-sized quartz and feldspar grains, with clay in between and shows three main pore types: (i) large pores (>10 μm) between quartz and feldspar grains; (ii) smaller pores (<1 μm) in the clay matrix; (iii) intragranular pores in the quartz and feldspar grains. Most of the pores are in the clay matrix, but the larger pores occupy most of the porosity; the intragranular porosity is minor, isolated, and was therefore interpreted as fluid inclusions (Hemes *et al.* 2013).

The other two samples are from hydrocarbon-producing geological formations, and shale gas plays from the Upper Jurassic Haynesville and Bossier Formations, cored in western Louisiana, USA. These organic-rich shales were deposited in a low-energy marine environment under mostly dysoxic conditions after each other during the opening of the Gulf of Mexico Basin, with the Bossier Shale being the younger one (Hammes & Frébourg 2012). The samples were cored at large depth (Table 1) and are tighter than the other two samples investigated. The Haynesville Shale sample (SOM 4-4) is a silty calcareous mudstone, with a relatively high total organic content (TOC) of 5.0 wt. %; its microstructure consists of large (>20 μm) carbonate grains with mostly intraparticle pores, quartz grains, a clay-rich matrix with interparticle pores that account for more than half of the porosity, organic matter containing secondary porosity, and pyrite with intercrystalline porosity (Klaver *et al.* 2015). The Bossier Shale sample (SMY 4-2) is a calcareous mudstone with a TOC of 1.1 wt. %. The microstructure consists almost exclusively of large calcite grains of about 50 μm in size with intraparticle pores and minor amounts of porous organic matter and clayey matrix in between the large grains that lack a clear preferred orientation (Klaver *et al.* 2015). From the same work, it follows that for both samples, the pores are several micrometers in size or smaller and that the pores in the Haynesville Shale have a more preferred orientation, subparallel to the bedding. Subsamples for the MIP and WMI experiments were taken less than a few cm apart from each other and were macroscopically the same for the Haynesville and Bossier Shale samples.

The four samples show a wide range in clay contents, porosity (Table 1), grain size, and framework type

(grain- versus matrix-supported). The average grain size decreases in the following order: Boom Clay, Bossier Shale, Haynesville Shale, and Opalinus Clay. The Bossier Shale and Boom Clay, to some extent, samples are grain-supported, whereas the Haynesville Shale and Opalinus Clay are matrix-supported. The Haynesville Shale sample is the richest in organic matter. All samples were stored dry in an exsiccator under vacuum and with silica gel.

Wood's metal injection

Wood's metal injection, such as MIP, is based on the capillary law for nonwetting liquids: $D = -4 \cdot (1/P)\ \gamma \cos \varphi$ (Washburn 1921), where D is the pore throat diameter (m), P the capillary pressure (Pa), γ the surface tension of the fluid (N m^{-1}), and φ the wetting angle (degree) (Urai *et al.* 2008). Thus, the amount of metal entering the sample at a given pressure is equal to the pore volume accessible through pore throats with the corresponding diameter.

Our WMI apparatus (Fig. 1A) consists of a pressure cell and two pistons, external heating, a thermocouple to measure the temperature, and a support for gently pushing the solid WM containing the sample out of the vessel after the experiment. The pressure cell was loaded in a manually controlled hydraulic press (max. 10 ton), equipped with a pressure gauge.

For the WMI experiment, the pressure vessel was heated to approximately 75°C and the WM melted in the pressure cell with the bottom piston in place. Prior to the WMI experiment, the Opalinus Clay and Boom Clay samples were oven-dried at 80°C for 24 h. The dry samples were immersed in the molten metal (Fig. 1A), and the top piston was put in place. The metal pressure was increased by 10–20 MPa, in time steps of 10 min, to a maximum of 316 MPa, in approximately 4–5 h (Fig. 1B). Taking an interfacial tension of 0.420 N m^{-1} and a wetting angle of 140° (Abell *et al.* 1999; Hildenbrand & Urai 2003), this pressure corresponds to a pore throat diameter of 4.1 nm (Washburn 1921). After the maximum pressure was reached, the heating was turned off, and, after letting the system cool down over night, the pressure was released and the solidified WM cylinder (containing the samples) was pushed out of the pressure cell. The samples were then mechanically cut out of the WM (at room temperature). Afterward, the injected rock samples were prepolished dry, using silicon carbide papers (down to grit 2400 see Houben (2013) for details), to prepare them for ion polishing.

Ion polishing and SEM Imaging

Cold BIB polishing

It is known from literature (e.g., Viguier & Mortensen 2001; Park *et al.* 2007) that samples heat up during ion beam milling. Our initial WMI-BIB-SEM observations also suggested melting of the alloy (Houben 2013), during BIB milling. In this study, we used an Argon ion beam polisher (Technoorg SC-1000), equipped with a Peltier module for keeping the sample temperature below 40°C during ion polishing. To create large planar polished sections of about 1 cm^2, the samples are rotated during low angle (6–9°) Argon ion bombardment. We applied the following configuration steps, using a focused high-energy ion source (FHEG) for polishing and a focused low-energy ion source (FLEG) for final cleaning. In the FHEG mode, an incident angle of 6° was used for 90 min, with an anode voltage of 10 kV and a focus voltage of 5 kV. In the FLEG mode, two different voltages were applied, both at an incident angle of 9° for 15 min, but first with an anode voltage of 1 kV and a focus voltage of 0.7 kV, and secondly using an anode voltage of 0.4 kV and a focus voltage of 0.28 kV.

SEM imaging

After ion polishing, the samples were investigated using a Zeiss Supra 55 field-emission SEM at RWTH Aachen University. This SEM is equipped with a SE2- and a SE-inlens detector for morphological analysis, a BSE detector for imaging density-phase contrasts, and an EDX detector (X-Max80 SDD-Detector; Oxford Instruments) for elemental analysis. This system can resolve features down to 5 nm (Houben 2013).

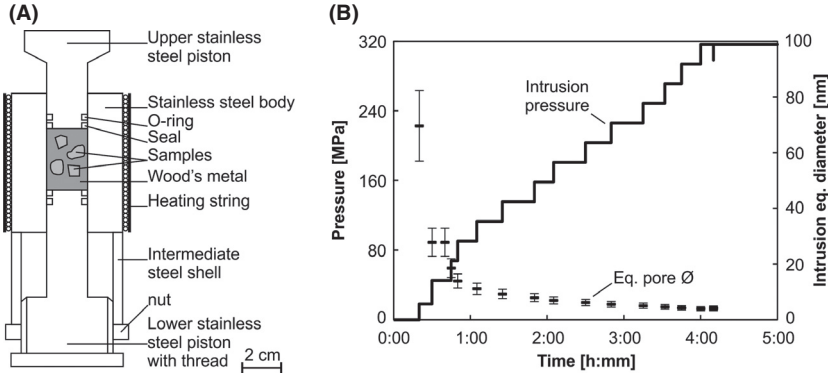

Fig. 1. Wood's metal injection. (A) Setup pressure cell used for the WM injection (after Hildenbrand & Urai 2003). (B) Diagram showing the incremental pressure steps and the equivalent pore throat diameters of a representative WM injection experiment. Left *y*-axis is the WM pressure and the right *y*-axis is the equivalent pore throat diameter versus the time on the *x*-axis.

MIP

For comparison with WMI results, MIP was performed at Micromeritics Analytical Services Europe (Aachen, Germany), on each of the four samples. Mercury intrusion and extrusion analyses were performed in the 360–0.003 micrometer pore throat range. Pore throat diameter distributions were calculated based on Washburn's equation (Washburn 1921) using a contact angle of 130 ° and a surface tension of 0.485 N m^{-1}. Mercury extrusion takes place at decreasing pressure steps. The differences between mercury intrusion and extrusion volumes give the mercury volumes trapped inside the samples, due to high pore body to pore throat size ratios and variable contact angles. The MIP data of the Boom Clay (silt-rich), Opalinus Clay (shaley facies), and Bossier Shale samples are from previous research (respectively Hemes *et al.* 2013; Houben *et al.* 2013; Klaver *et al.* 2015; see also Table 1). Before the MIP experiments, the Opalinus Clay, Boom Clay, and Haynesville Shale samples were dried at 80°C for at least 96 h. The Bossier Shale samples were predried at room temperature in high vacuum (1×10^{-3} to 1×10^{-4} Pa) for 30 h.

RESULTS

WMI–BIB–SEM

The overall microstructure and pore morphology of the BIB-milled sections does not vary significantly from the general microstructure observed in previous studies (Hemes *et al.* 2013; Houben 2013; Klaver *et al.* 2015). Scratches from mechanical polishing are not visible on the sample surfaces; the thickness of the sample surface removed during BIB milling is at least in the order of several micrometers (average particle diameter of the SiC paper is 10 μm). The WM is visible by the light gray values in the BSE images, because of its higher density.

Opalinus Clay

In the Opalinus Clay sample investigated, WM is mostly found in the cracks (Fig. 2A), but major parts of the matrix were not filled (Fig. 2A–C), with the exception of one layer impregnated with WM (Fig. 2A). The filled cracks are subparallel to the bedding and tend to follow large carbonate grains interpreted as bivalve fragments (Klinkenberg *et al.* 2009; Houben 2013). Larger pores in some pyrite framboids and carbonate fossils which are close to or in contact with filled cracks are also filled with WM (Fig. 2B), cf. Houben (2013). Most of the matrix pores, even the ones close to cracks, do not contain WM (Fig. 2B). Also, some cracks show a discontinuous WM fill (Fig. 2C) which is an artifact of the WM and will be discussed in Wood's Metal. The smallest filled pore, imaged in this cross section is about 10 nm in diameter (Fig. 2D).

Boom Clay

Observations in the SEM show that the large pores in the Boom Clay sample are almost completely WM-filled (Fig. 3A). In contrast, some of the pores in the clay-rich matrix are not filled at all, or only partly filled (Fig. 3B). In the same figure, elongated pores, interpreted as open cracks, are not filled with the WM Unfilled regions tend to be elongated between impregnated regions in the clay matrix, containing both, unfilled meso- and macropores (Fig. 3B and C). High-resolution SEM imaging has confirmed WM in pores down to 10 nm in diameter (Fig. 3D).

Haynesville Shale

In the Haynesville Shale sample, the majority of WM is found in cracks connected to the edges of the sample (Fig. 4A). Cracks are common in this sample, at a low angle to the bedding and locally bending around larger carbonate grains. WM is found in the clay-rich matrix, <10 μm from the cracks, but the majority of the matrix pores does not contain WM (Fig. 4B). Some small (<μm) cracks are not filled with WM. Interparticle pores filled with WM can be seen in between an uncommon aggregate of randomly stacked clay sheets (Fig. 4C). Also in this sample, pores down to 10 nm contain WM (Fig. 4D).

Bossier Shale

In the Bossier Shale sample, about half of the area of the cross section does not contain WM at all, whereas the other half shows full impregnation with the alloy (Fig. 5A). The impregnated regions are up to 500 μm wide and subparallel to the bedding. Typically, the interparticle pores in clay or organic matter between carbonate grains, which are filled, are larger (up to 5 μm) in the impregnated regions, than the unfilled intraparticle pores (<1 μm) (Fig. 5B and C). EDX analysis indicates that the nonimpregnated regions have relative low counts of typical clay elements (Al, Si and K), but relative high counts of Ca. Again, the smallest WM-filled pores in this sample are approximately 10 nm in width (Fig. 5D).

Wood's metal

The WM surrounding the samples and the WM in the pores showed no evidence of remelting during ion milling. Other WM samples, from earlier investigations, polished using BIB milling without cooling, resulted in clear visible remelt of the surrounding WM and mm-sized WM bubbles on the sample (Fig. 6A, I, and II). On three ion-milled samples, locally, a few WM bubbles were observed along the sample edge not covered by the WM (Fig. 6B–D), indicating remelting of the WM. Along these sample edges, the ion beam interacts with the low thermally conductive sample material at an high angle (approximately 84°), resulting in local melting of the WM. Moreover, it turned out that the WM reacts with the gold coating on the sample surface

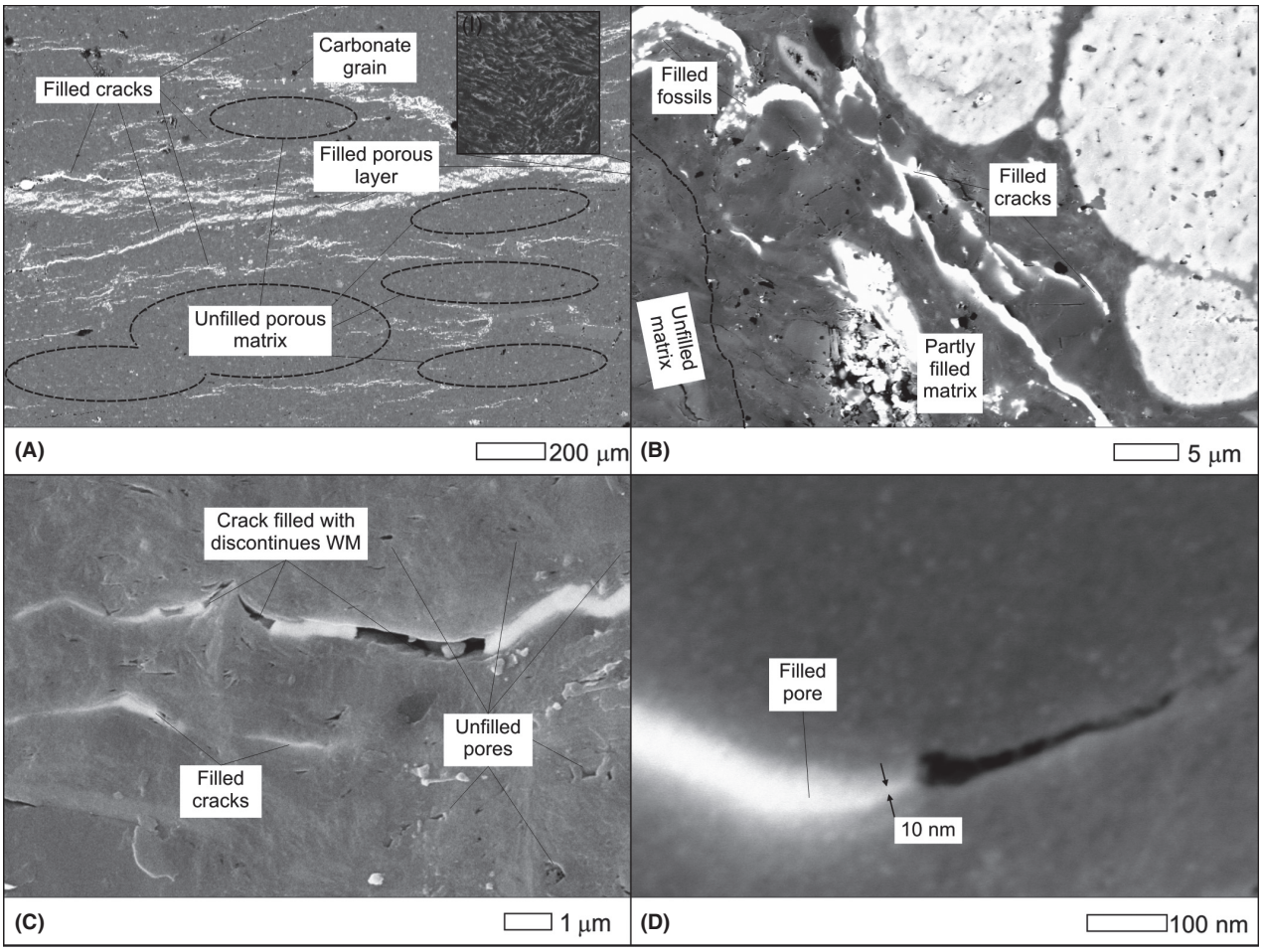

Fig. 2. SEM images of WM in Opalinus Clay. (A) Overview of the OC showing the WM mainly inside the cracks and in one porous layer (pop-up). (B) WM-filled fossils and partly filled matrix along the filled cracks. (C) Unfilled matrix along a discontinues crack fill. (D) The smallest WM-filled pore (tip) encountered in the sample at the highest magnification.

(Fig. 6E and F) because the uncoated samples do not show these dendrite structures on top of the WM. This is an ongoing process since after several months, the effect of the reaction is more intense (Fig. 6F, right side). Also, cavities and cracks (Fig. 6G and H), exist in the WM, as well as phase segregation of the WM (Fig. 6I). EDX analyses indicate that the WM segregates in at least five different phases: (i) Sn; (ii) Cd; (iii) Cd + Sn; (iv) Bi + Pb; and (v) Bi + Pb + Sn. In the Sn phase, pores of micrometer size were found (Fig. 6J–L); thus, pores or cavities imaged within the WM, (e.g., Fig. 6G) were interpreted to be in the Sn phase of the WM. Observed cracks and other cavities are interpreted to exist because of several reasons:

(1) Nonisothermal solidification (Yadav *et al.* 1987) and related phase segregation into its constitutive metals; initiating differential shrinkage during cooling.
(2) The subsequent pressure release initiating cracks along the constitutive metals that have different elastic moduli.
(3) Over-pressured air (Hildenbrand & Urai 2003) and residual water in the sample, potentially filling the cavities in the WM as impurities. However this effect will be minor as, because of their lower viscosity, the air and water would be displaced into the smaller pores, which are too narrow for the WM to enter. Besides, the volume of the compressed air will be small as air will be compressed to 0.14% of its original volume, by increasing the pressure from atmospheric conditions to 316 MPa at 90°C.
(4) There exists the possibility of differential WM shrinkage, and that poorly connected WM casts are physically pulled out of the sample by the mechanical prepolishing. However, this would only apply to the poorly connected large (> several micrometers) WM bodies, because the BIB milling removed the damaged surfaces containing scratches and pull-out structures from the mechanical polishing.

MIP

Unprocessed MIP data of the Opalinus Clay and the Haynesville Shale samples show that mercury intrusion

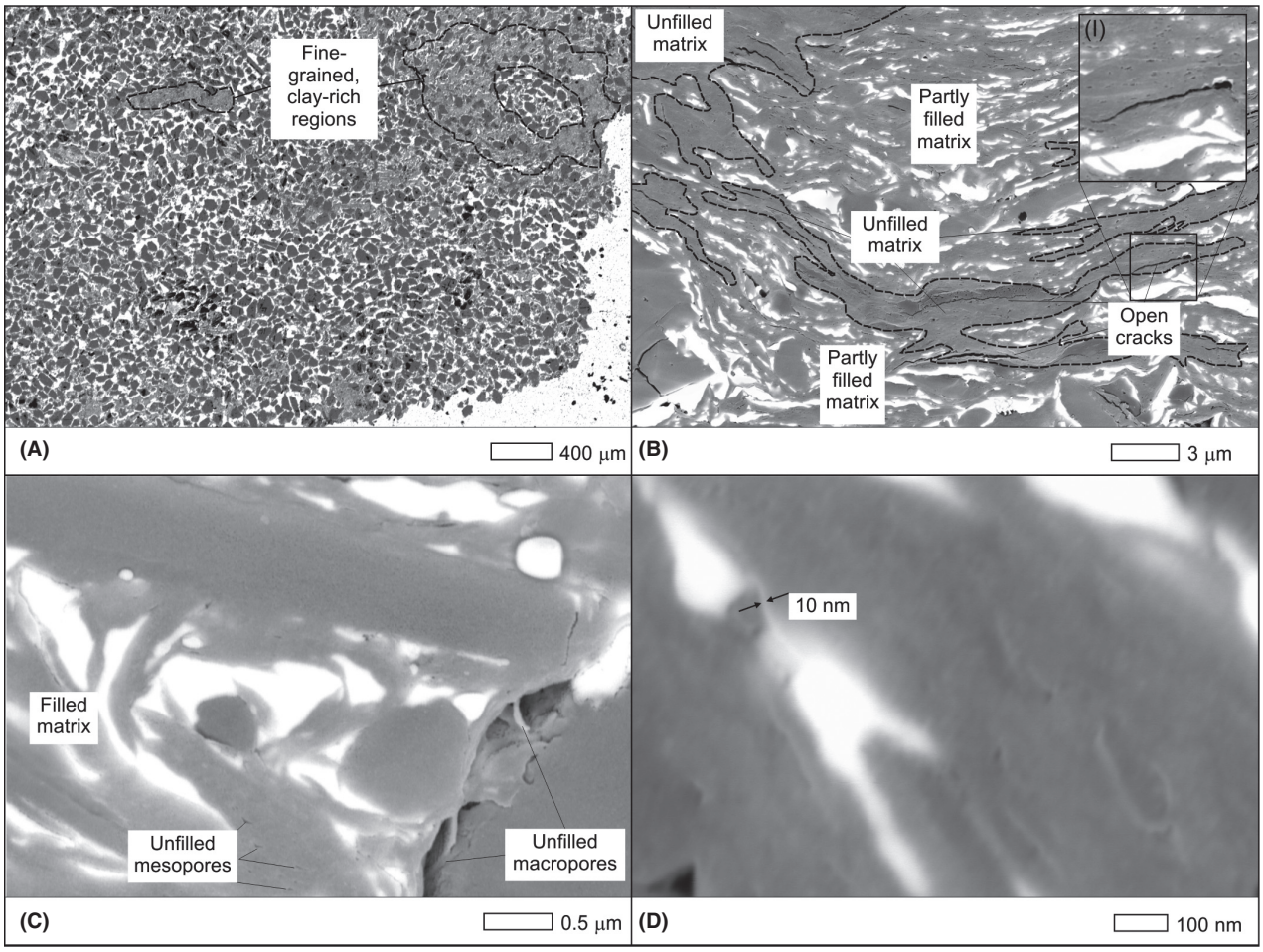

Fig. 3. SEM images of WM in Boom Clay. (A) Overview of the BC showing the WM throughout the whole ion-polished section. (B) Partly WM-filled matrix inside the fine-grained, clay-rich regions, indicated in (A). (C) Filled pores in the clay and unfilled meso- and macropores. (D) The smallest WM-filled pore width encountered in the sample at the highest magnification.

starts at pressures equivalent to pore throats ≫5000 nm, corresponding to 3.2% and 0.7% porosity, respectively. Apart from the Boom Clay, pores of this size were never observed in the samples investigated (Hemes *et al.* 2013; Houben *et al.* 2013; Klaver *et al.* 2015) and these data were therefore interpreted as filling of cracks, which are clearly present in the samples (Figs 2 and 4), or surface roughness, and were not included in the interpretation of pores. Therefore, the MIP data were cut off at 1, 30, and 5 μm for the Opalinus Clay, Boom Clay, and Haynesville and Bossier Shale samples, respectively. Results of all MIP experiments are shown in Fig. 7.

The connected MIP porosity measured for Opalinus Clay is 13.0%, and after extrusion, the sample shows a trapped porosity of 7.1% (Fig. 7A). The intrusion curve indicates a gradual intrusion from the beginning down to about 50 nm. Most of the intrusion took place from 50 nm onwards. At 20 nm, the intrusion rate is the highest (Fig. 7A).

For the silt-rich Boom Clay sample, MIP shows a major intrusion above 1000 nm, corresponding to about 80% of the total intrusion volume (Fig. 7B). Another 20% is intruded in the submicron pore-size range, adding up to a total connected porosity of 32.2%. A significant amount of mercury (29.7%) remained trapped inside the sample, after the extrusion.

The MIP curve of the Haynesville Shale sample indicates mercury intrusion mainly in the range from 100 nm, down to 3 nm (Fig. 7C). Most of the intrusion occurred below 15 nm, with highest intrusion rates at 6 nm (Fig. 7C), cumulating in a total connected porosity of 2.9%. Extrusion occurred only at pressures equivalent to pore throats above 300 nm, resulting in a trapped porosity of 2.7%. This is significantly smaller than the total MIP porosity (9.2%, Klaver *et al.* 2015) and is attributed to a combination of possible different drying conditions, MIP artifacts, cracks, and sample heterogeneity.

The MIP results of the Bossier Shale sample show that most of the intrusion took place at high pressures, equivalent to pore throats smaller than 10 nm (Fig. 7D). The strongest intrusion occurred at a pressure equivalent to

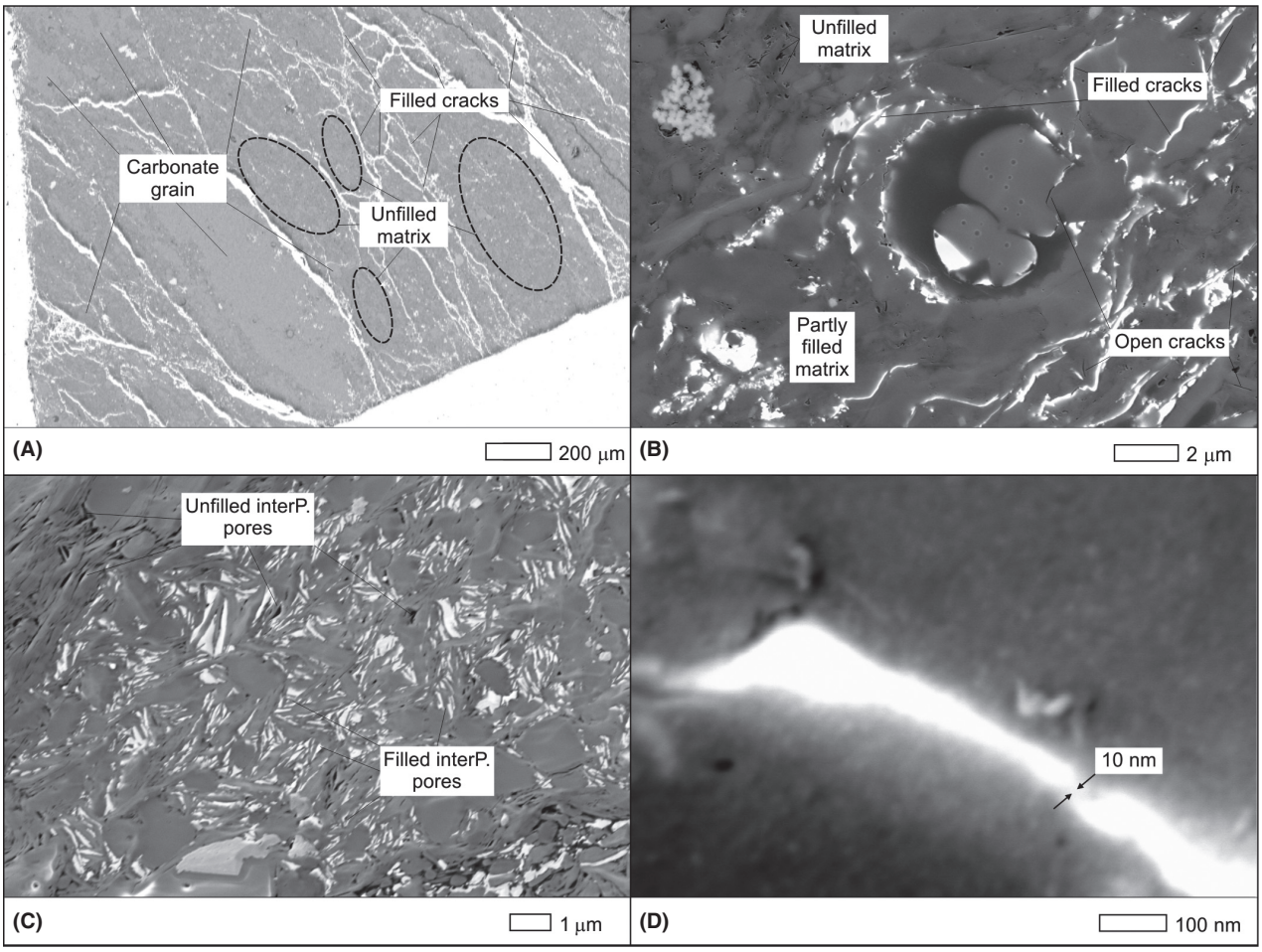

Fig. 4. SEM images of WM in Haynesville Shale. (A) Overview of the HS showing the WM mainly inside the cracks that cross-cut the whole ion-polished section. (B) Partly WM-filled matrix adjacent to a WM-filled crack. (C) Filled interparticle pores between clay sheets. (D) The smallest WM-filled pore width encountered in the sample at the highest magnification.

4 nm pore throat diameter (Fig. 7D). In total, the connected porosity is 2.2%. Extrusion happened only at pressures equivalent to pores larger than 10 nm. The gap between intrusion and extrusion curve indicates that roughly half of the mercury is trapped inside the sample, equivalent to 1.2% porosity.

DISCUSSION

Wood's metal injection into fine-grained geomaterials

It is known from transmission electron microscopy sample preparation that during ion milling, samples can reach temperatures of 400 to 330°C, respectively (Viguier & Mortensen 2001; Park *et al.* 2007;). However, these ion milling operations were performed on smaller samples (about 10 times thinner) and at a higher milling angle (2–3 times higher). On the other hand, it is evident from Fig. 6A that WM also melts during conventional BIB milling without using the Peltier module. Therefore, all WM-injected samples were ion-milled using a rotating sample holder equipped with a Peltier cooling module, to keep the temperature of the samples below 70°C, during ion polishing. As the WM has a high thermal conductivity and it forms a continuous heat-conductive path between the cooled sample holder and the ion-milled surface, we expect that this is sufficient to not melt the WM during ion milling. This is also demonstrated by the Boom Clay sample which shows virtually a full impregnation of the WM after the ion milling. Except along some edges of the ion-polished surface that were not protected by the WM, it could be that along these edges, the WM melted out of the pores during ion milling. All other regions of the ion-milled surfaces show no evidence of remelting of WM during ion milling (Figs 2–5). However, there remains the possibility that small thermally isolated WM pore fillings could melt due to poor thermal conduction. Overall, we conclude that in our samples, BIB polishing did not change the main structure of the injected alloy in the pores.

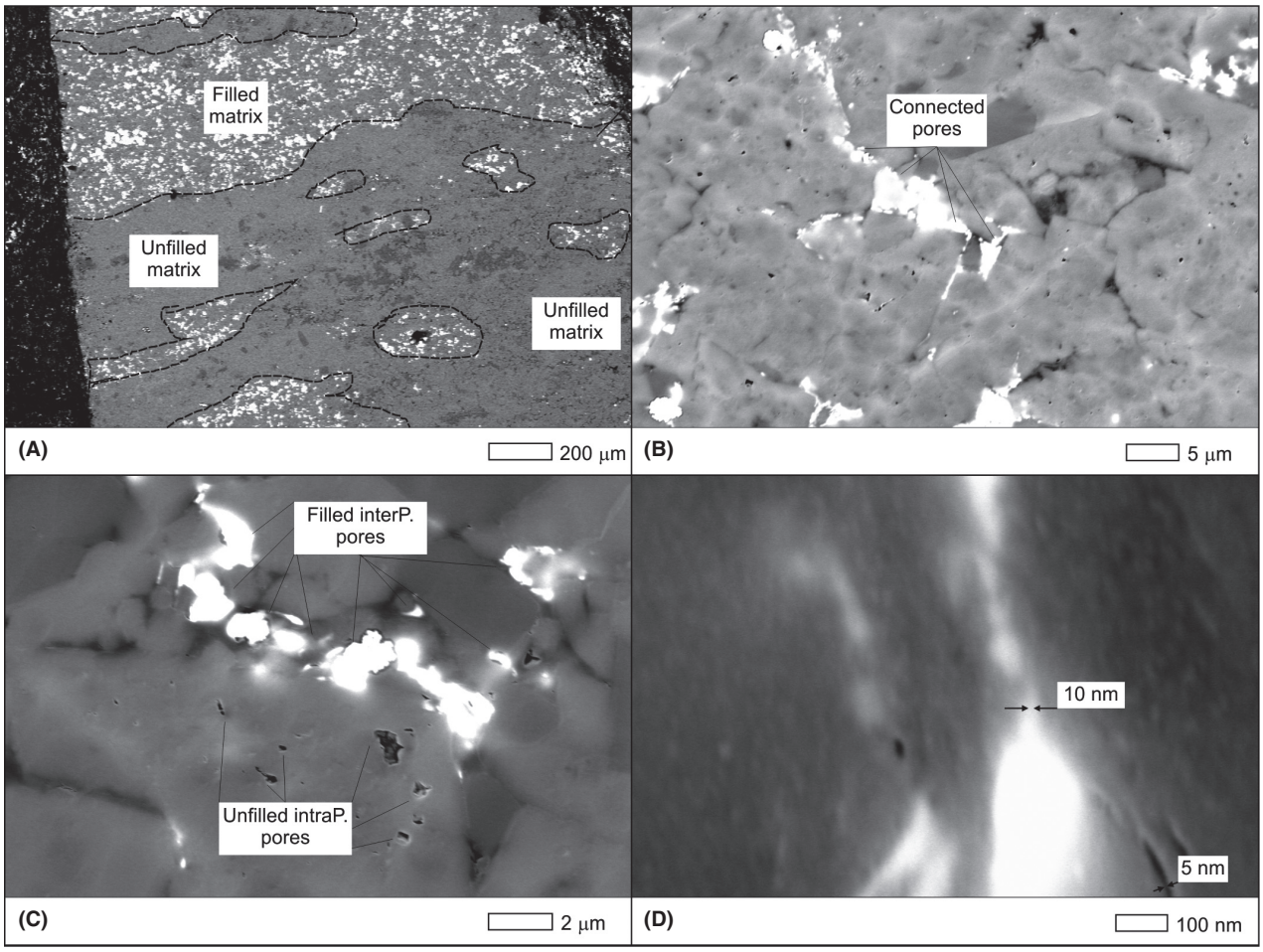

Fig. 5. SEM images of WM in Bossier Shale. (A) Overview of the BS showing the WM-filled and unfilled regions. (B) The WM in the impregnated regions illustrates the connected pores between the carbonate grains. (C) Filled interparticle pores versus unfilled intraparticle pores. (D) The smallest WM-filled and unfilled pore width encountered in the sample at the highest magnification.

In all four samples, the smallest WM-filled pores imaged by SEM are about 10 nm in diameter (Figs 2–5). This shows that the nonwetting WM has been able to intrude small pores, and moreover, that WMI is a powerful method to quantify connected porosity in 2D sections. On the other hand, using Washburn's equation, a capillary pressure of 316 MPa, a surface tension of 0.420 N/m, and a wetting angle of 140°, pores down to 4 nm should be filled, in theory. Possible reasons for this discrepancy between the imaged smallest WM-filled pores and the theoretically reached smallest WM-filled pore diameters are as follows:

(1) Deviations of published physical properties of molten WM; published surface tensions of WM vary from 0.40 to 0.49 and wetting angles vary between 130 and 140° (Willis *et al.* 1998; Abell *et al.* 1999; Nemati 2000; Darot and Reuschlé, 2003; Hildenbrand & Urai 2003; Lloyd *et al.* 2009; Galaup *et al.* 2012), resulting in possible pore throat entry diameters at 316 MPa, between 3.3 and 4.7 nm, a relatively small variation (see whiskers in Fig. 1B). It is unknown how many WM properties vary with respect to the pore space mineralogy. The WM has been observed in contact with quartz, organic matter, clay, and carbonate.

(2) WM in shale samples is bright in BSE images, compared to the clay matrix, and an accurate measurement of the sizes of small amounts of WM in pores at high magnifications (up to 350 000×) (Figs 2–5D) is difficult. Future work is aimed at resolving this more accurately.

(3) It is possible that the samples did contain smaller WM-filled pores, but we did not find them in the imaged areas.

(4) It is possible that the WMI experiment was performed too fast and the pressure of the liquid WM was not in equilibrium everywhere and needed more time to penetrate the smallest pores. Yadav *et al.* (1987) mentioned 1.33 mPas which is comparable to the viscosity

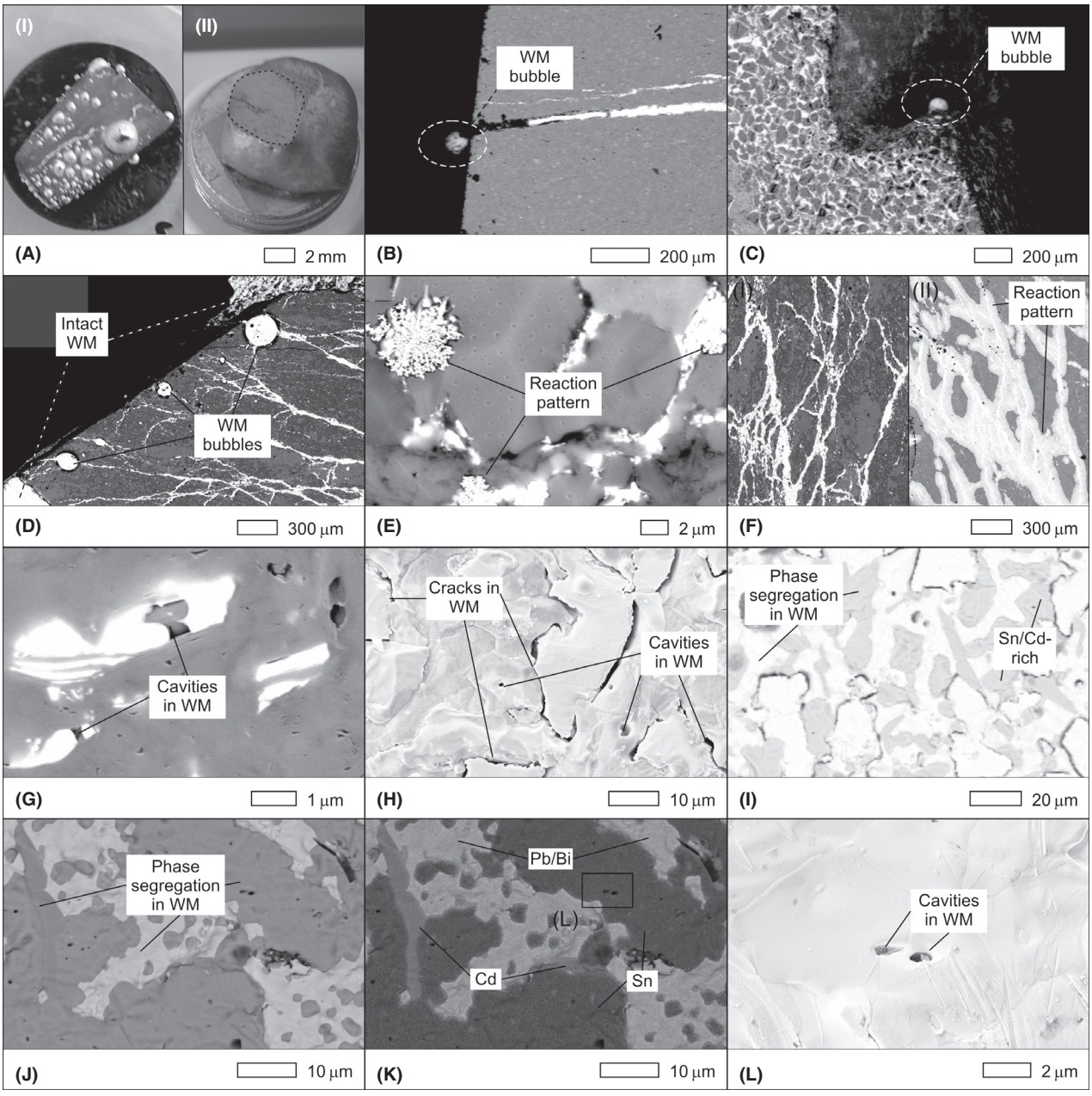

Fig. 6. SEM images of WM remelt and artifacts. (A) Remelt of WM because of ion milling without using a Peltier module for cooling indicated by: (I) mm-size bubbles on a sample without surrounding WM; or (II) smooth WM edges enclosing a sample. (B;C;D) Local WM bubbles at the edge of the polished sections not covered by the WM, indicating local remelting of the WM. The intact WM at the sides of the sample in (D) indicates no remelt of the enclosing WM. (E) Typical oxidation pattern on top of the WM-filled pores. (F) Intense oxidation of the WM on top of the polished section after 5 months (II) of exposure to air. (G and H) Cavities and undulating cracks in the WM. (I) Phase segregation of the WM (the darker phase is enriched in Sn and Cd). (J) BSE images illustrating the phase segregation of the WM and pores inside the Sn phase (K) EDX-layered image showing the Cd, Pb/Bi, and Sn phases. (L) SE2 image showing pores of about 1 μm in the Sn phase.

of mercury, but Darot & Reuschlé (1999) found a significant increase in viscosity at 85°C. Accordingly, our WMI experiments took longer (4–5 h) than the MIP experiments (minutes to a few hours) estimated as sufficient to reach equilibrium. We note that if the viscosity would have been an issue, we would have seen a gradual decrease in the degree of impregnation of WM from the sides of the samples to their centers, which is not the case (Figs 2–5). Still, it is worth considering doing WMI and MIP experiments over a longer time span to ensure maximum saturation in these low permeable rocks.

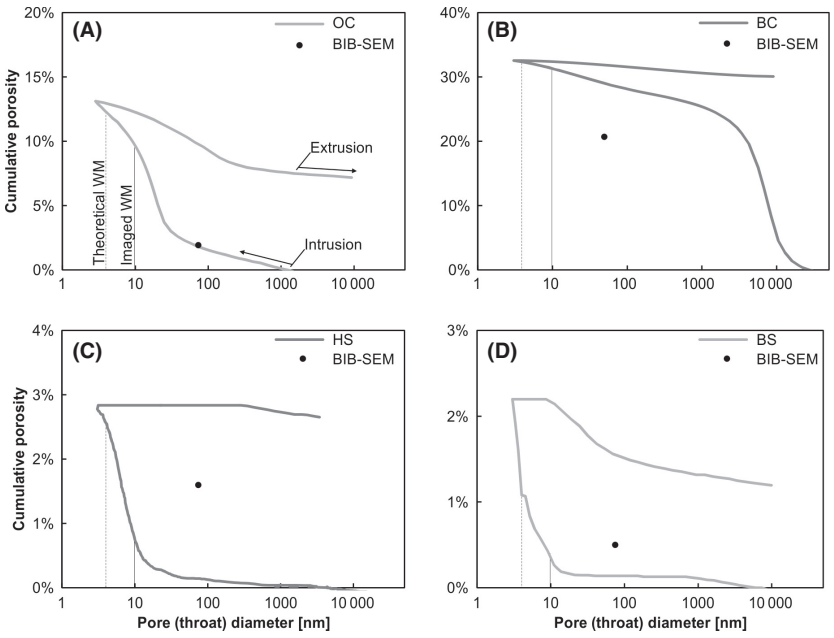

Fig. 7. MIP intrusion and extrusion curves showing the cumulative porosity versus pore (throat) diameter of the Opalinus Clay (A; after Houben *et al.* (2013)Houben *et al.* (2014b); cutoff >1 μm), Boom Clay (B; after Hemes *et al.* (2013); cutoff >30 μm), Haynesville (C) and Bossier Shale (D) (cutoff >5 μm for both). The lower curve is the intrusion measurement and the upper curve is the extrusion measurement for each MIP cycle. The solid vertical lines in the diagrams illustrate the pore throat diameters imaged in the SEM and the dashed vertical lines the theoretical minimal pore throat diameter achieved during the maximum injection pressure (= 4 nm). The visible BIB-SEM porosities are also given for the samples and are obtained from other studies (see also Table 1).

(5) Oxidation of the WM surface or some other reaction of the metal with the matrix (Kuhn *et al.* 1962) could have hindered intrusion. We have not found any evidence of oxidized films (in the WM-filled pores) and they have also not been reported in other studies (e.g., Dullien 1981; Nemati & Monteiro 1997; Nemati 2000; Lloyd *et al.* 2009).
(6) The pores are closed off by effective stresses (will be discussed in Deformation of rock due to MIP and WMI)
(7) The small pores are simply not connected with pore throats accessible to the molten metal.

In summary, from the comparable wetting properties and viscosity we assume that WMI resembles MIP (Dullien 1981; Abell *et al.* 1999) and WMI in combination with BIB-SEM is a method to analyze at high resolution which parts of a sample have been intruded by the alloy. We conducted WMI experiments, similar to earlier work described in the literature, but at higher pressures and with a much better resolution of the metal-filled nanopores. We also conclude that pore throats smaller than 10 nm in diameter were intruded by the metal. WMI provides new insights to the dimensions and geometries of pore networks, which are connected by pore throats corresponding to the capillary pressure. Moreover, it shows that in each investigated sample, a significant volume of larger pore bodies is not connected via pore throats down to around 10 nm (in diameter). In the analyzed Boom Clay sample, larger pores form a connected backbone, but a part of the pore space within the fine-grained clay matrix is not connected. In the Bossier Shale sample, the connectivity is very heterogeneous and only about half of the pores are connected.

Comparison of WMI-BIB-SEM and MIP results

Samples used for the WMI-BIB-SEM and the MIP experiments do not originate from exactly the same sample volumes; thus, a direct comparison of the two analyses is only possible if the samples are similar. The SEM images (Figs 2–5) of our samples are indistinguishable from sample descriptions in Sample description, observed in previous studies, illustrating the low variability of microstructures between the samples.

Comparing results of the BIB-SEM observations on WM-injected samples (Figs 2–5) to MIP data (Fig. 7) shows some disagreement for the Opalinus Clay and the Haynesville Shale samples, whereas for the silt-rich Boom Clay and the grain-supported and less porous Bossier Shale samples, there is a good agreement between the mercury intrusion curves and the WM-filled pore space observed in SEM images. In Opalinus Clay, according to the MIP intrusion curve, at least two-thirds of the porous network should be filled with WM (Fig. 7A), corresponding to pores >10 nm in pore throat diameter. However, from SEM observations, WM is only visible in the cracks, crack adjacent fossils, and one exceptionally porous layer, whereas the majority of the clay matrix is not accessible to the WM. On the other hand, the porous layer and cracks account for approximately 90% of the total resolved porosity in the Opalinus Clay sample are investigated. In the Haynesville Shale sample, WM is almost only visible in the cracks, while MIP suggests that intrusion also took place

above 10 nm pore throat diameter, but with a maximum intrusion at 6 nm pore throat diameter. For the silt-rich Boom Clay, the SEM image (Fig. 3A) shows an almost entirely filled and thus interpreted as entirely connected pore space, which is in good agreement with the MIP intrusion curve (Fig. 7B). Only in some fine-grained, clay-rich regions, the pore space is not entirely filled with WM. In the grain-supported, coarse-grained, and less porous Bossier Shale sample, WM clearly intruded the rock fabric in a (mm-scale) layered manner. This intrusion probably took place via pore throat diameters of approximately 4 nm, in agreement with the maximum intrusion during MIP. The unfilled regions are most probably more cemented and unconnected above pore throat diameters of 4 nm and thus isolated at the scale of observations.

The higher visible BIB-SEM porosities, compared to MIP data (about four to ten times; Fig. 7C and D), at comparable resolutions, indicate high pore body to pore throat ratios for the Haynesville and Bossier Shale samples. For the Opalinus Clay (shaley facies) sample, the porosity measured by BIB-SEM fits the porosity measured by MIP at a corresponding resolution (Fig. 7A), indicating an interconnected cylindrical pore space in Opalinus Clay, however, with the connecting pore throat diameters below the resolution of published SEM-studies on representative Opalinus Clay samples (Keller *et al.* 2011, 2013b; as well as Houben *et al.* 2013, 2014b). For the Boom Clay sample, the porosity measured by BIB-SEM (Hemes *et al.* 2013) is clearly below the porosity measured by MIP at a comparable resolution (Fig. 7B), interpreted as a nonrepresentativeness of the area investigated using BIB-SEM, or an overestimation of the porosity measured by MIP, due to filling of cracks and/or surface roughness effects. An additional process preventing the flow of WM into the connected pore space is the closure of pore throats by compaction of matrix porosity, caused by effective pressures generated by capillary resistance. We will discuss this in more detail, below.

Deformation of rock due to MIP and WMI

It has been reported before that geomaterials can be compressed during MIP (Penumadu & Dean 2000; Giesche 2006; Yao & Liu 2012), due to the capillary resistance allowing the metal to create an effective confining pressure around unfilled regions of a sample. This process is enhanced by anisotropy, for example, due to lamination or cracks. Compaction of samples can be elastic and inelastic, and composed of closure of microcracks, compression of the matrix, and compression of the minerals. Deformation, in particular elastic deformation, might be highest in samples, which are highest in organic matter or clay. Considering the maximum intrusion pressure of 414 MPa and bulk moduli of 6.7 GPa for organic matter (Zeszotarski *et al.* 2004), 20.9 GPa for clay (Mavko *et al.* 2009), and 38 GPa for quartz (Carmichael 1989), the elastic strains are 4.1% for organic matter, 1.3% for clay, and 0.7% for quartz, respectively. Plastic deformation is attributed to pore collapse (Dewhurst *et al.* 1998) or crack closure caused by effective pressures generated by capillary resistance during MIP or WMI (Fig. 3B).

To quantify the amounts of elastic and plastic deformation, one could run a blank MIP experiment with a coated sample or nonporous sample (Penumadu & Dean 2000; Sigal 2009). Such an experiment measures the potential maximum deformation of the sample but not the deformation during mercury intrusion. In this study, MIP experiments were carried out on epoxy-coated samples; however, it turned out that the epoxy was permeable for the WM and therefore most likely also for the mercury (these are not discussed in this study).

Our results suggest that MIP on fine-grained, anisotropic rocks may contain large artifacts of sample deformation and crack filling, which cannot be corrected for using MIP data alone. A correct interpretation of pore-size distributions from MIP requires confirmation, for example, by direct observations of the metal-filled pore space, using WMI-BIB-SEM, as presented in this study.

Model

For fine-grained, clay-rich rocks that may contain cracks, we summarize the above discussion by proposing the occurrence of compacted clay-rich regions and unfilled porous regions between filled cracks and compressed grains, during MIP and WMI (Fig. 8A–C). The conditions and processes associated with the interpreted inelastic and elastic deformations are presented in Fig. 8B and C, including anisotropies of the material, such as bedding or cracks, which control the preferred intrusion pathways, and may result in either accessing or cutting off of pore connections, due to potential compaction of the material at high pressures. It is clear, that in the Opalinus Clay and Haynesville Shale samples, the WM entered the rock matrix from cracks, which run subparallel to the bedding (Figs 2 and 4). In the silt-rich Boom Clay, unfilled porous regions exist in the clay matrix, between filled regions, as a result of inelastic deformation of the clay matrix, leading to a cutting off of pore pathways at high pressures (Fig. 3). In the Bossier Shale sample, the WM follows the anisotropies of the bedding, but in this case, the porous network controls the pathways (Fig. 5).

In a highly porous and permeable rock, saturated with a fluid at high pressure, the effective stress is zero, as the fluid pressure is equal to the confining pressure (Terzaghi 1925). During a WMI or MIP experiment, this situation may be approximated if the fluid can enter a backbone of the pore space at low pressure and fill smaller pores with

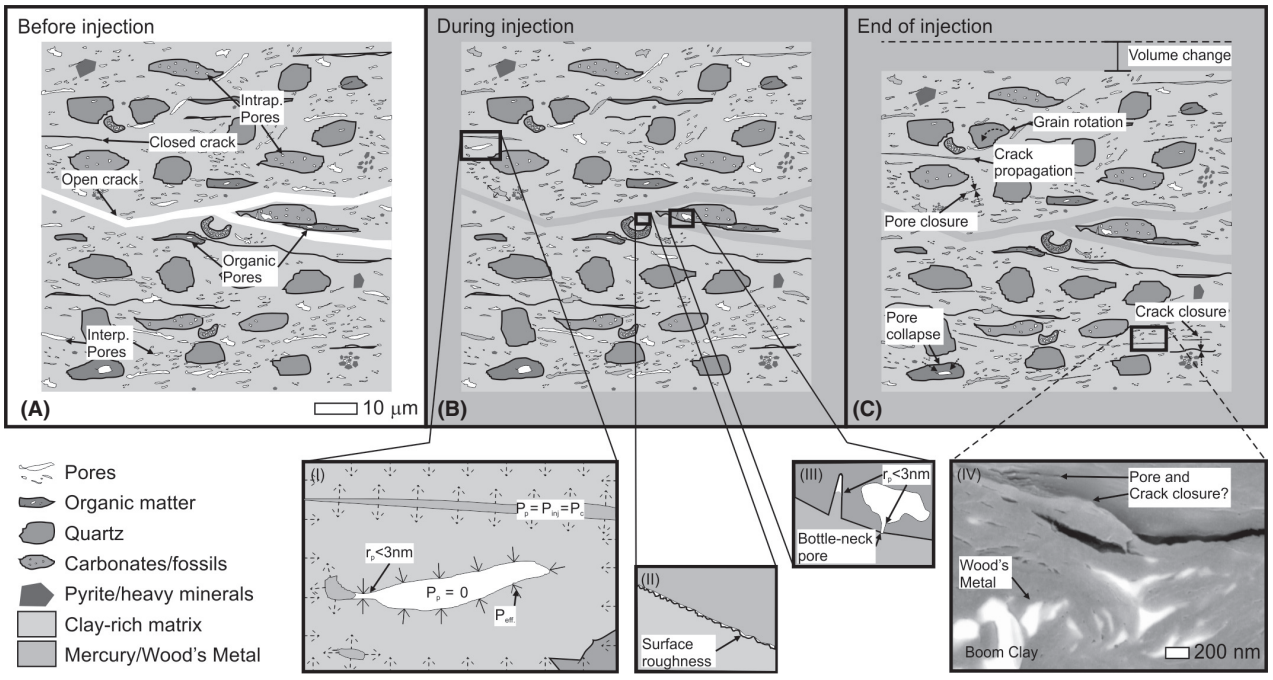

Fig. 8. WMI-MIP intrusion model. (A) Simplified model of a heterogeneous clay-rich shale with interparticle pores in the clay-rich matrix (gray), organic matter (brown), quartz (blue), and carbonate grains and fossils (green) with intra-particle pores and heavy minerals (red). Cracks are also indicated and are subparallel to the bedding. (B) Intrusion model of liquid mercury or Wood's metal, indicating the preferred injection through the cracks during the experiment. Details of processes during the intrusion are shown in the pop-ups (I, II, III); for more information, the reader is referred to the text. (C) Intrusion model of liquid mercury or Wood's metal at the end of the injection experiment. The processes that might have taken place in the sample during the injection are indicated. The pop-up (IV) shows an example SEM image of likely pore and crack closure in Boom Clay, due to the injection process.

increasing pressure. However, if larger volumes of a sample can only be accessed at high pressure, these volumes may be compacted to an unknown extent; this compaction cannot be detected from the MIP data alone. A similar process takes place as a result of preferential intrusion, due to anisotropies and cracks (Fig. 8B-(I)), which may cause inelastic deformation of the clay matrix, for example, bending or sliding of particles and closing of even smaller pore throats (Fig. 8B-(I), C). At increasing pressures, the serrated pore boundaries start to fill with the liquid metal (Fig. 8B-(I) but pores with throats smaller than 3 nm will not be filled at all (Fig. 8B-(I, III). This process will be particularly important in soft, clay-rich regions, as observed in the Boom Clay sample (Fig. 8C-(IV)).

CONCLUSIONS

On the basis of BIB-SEM observations on four WM-injected samples as well as MIP analyses on corresponding samples, we conclude the following:

(1) WMI is comparable to MIP as molten WM has comparable physical properties to mercury; and WMI in combination with BIB-SEM is a powerful tool to analyze at high resolution which parts of a sample are intruded by the liquid metal or alloy at mm to cm scale.

(2) High-pressure WMI in combination with high-resolution BIB-SEM provides new insights to the dimensions and geometries of pore networks in fine-grained rocks. It shows that in most of the samples, significant volumes of larger pores are not connected via pore throats down to about 10 nm in diameter. It appears that in particular for the Opalinus Clay sample, the pore throats are actually smaller than measured by MIP, resulting in a higher capillary resistance and thus a higher sealing capacity.

(3) MIP data of fine-grained rocks can contain significant artifacts, which cannot be corrected for using the MIP data alone. Pore-size distributions derived from MIP require confirmation by direct observations of the metal-filled pore space, for example, using the described WMI-BIB-SEM method. Also, it shows what part of the pore space in the sample forms the interconnecting pore network.

(4) Pore throats may be cut off during MIP or WMI, due to deformation and compaction of the clay matrix. Pore-size distributions measured by MIP may therefore also reflect deformation of the rock and not only the in-situ pore-size distributions. Moreover, this study follows that cracks play a major role during the intrusion of molten WM (or mercury) into the rock, indicating

that significant care should be taken during sample preparation.

ACKNOWLEDGEMENTS

The authors would like to thank Shell, Swisstopo, Nagra, and SCK-CEN for providing the samples. We thank Alexandra Amann from the Institute of Geology and Geochemistry of Petroleum and Coal at RWTH Aachen University, who helped with the setup of the first experiments. Comments by Stéphane Brassinnes (ONDRAF/NIRAS), Mieke De Craen (SCK-CEN), Calum Macaulay, and Henning Peters (Shell) are gratefully acknowledged. The financial support of Shell Global Solutions International B.V. and their permission to publish this article is highly appreciated. We thank P.J. Armitage and several anonymous reviewers for their helpful reviews of the manuscript.

REFERENCES

Abell AB, Willis KL, Lange DA (1999) Mercury intrusion porosimetry and image analysis of cement-based materials. *Journal of Colloid and Interface Science*, **211**, 39–44.

Armitage PJ, Worden RH, Faulkner DR, Aplin AC, Butcher AR, Iliffe J (2010) Diagenetic and sedimentary controls on porosity in Lower Carboniferous fine-grained lithologies, Krechba field, Algeria: a petrological study of a caprock to a carbon capture site. *Marine and Petroleum Geology*, **27**, 1395–410.

Busch A, Amann-Hildenbrand A (2013) Predicting capillarity of mudrocks. *Marine and Petroleum Geology*, **45**, 208–23.

Carmichael RS (1989) *CRC Practical Handbook of Physical Properties of Rocks and Minerals*. C R C Press, Boca Taton, FL, USA.

Chalmers GRL, Ross DJK, Bustin RM (2012) Geological controls on matrix permeability of Devonian Gas Shales in the Horn River and Liard basins, northeastern British Columbia, Canada. *International Journal of Coal Geology*, **103**, 120–31.

Clarkson CR, Solano N, Bustin RM, Bustin AMM, Chalmers GRL, He L, Melnichenko YB, Radliński AP, Blach TP (2013) Pore structure characterization of North American shale gas reservoirs using USANS/SANS, gas adsorption, and mercury intrusion. *Fuel*, **103**, 606–16.

Curtis ME, Ambrose RJ, Sondergeld CH, Rai CS (2010) Structural characterization of gas shales on the micro- and nano-scales. In: *Canadian Unconventional Resources and International Petroleum Conference* Calgary, Alberta, Canada, Society of Petroleum Engineers, SPE 137693, 15.

Darot M, Reuschlé T (1999) Direct assessment of wood's metal wettability on quartz. *Pure and Applied Geophysics*, **155**, 119–29.

Darot M, Reuschlé T (2003) Wood's Metal Dynamic Wettability on Quartz, Granite, and Limestone. *Pure and Applied Geophysics*, **160**, 1415–27.

Dewhurst DN, Aplin AC, Sarda J-P, Yang Y (1998) Compaction-driven evolution of porosity and permeability in natural mudstones: an experimental study. *Journal of Geophysical Research*, **103**, 651–61.

Diamond S (2000) Mercury porosimetry: an inappropriate method for the measurement of pore size distributions in cement-based materials. *Cement and Concrete Research*, **30**, 1517–25.

Dullien FAL (1981) Wood's Metal porosimetry and its relation to mercury porosimetry. *Powder Technology*, **29**, 109–16.

Dultz S, Behrens H, Simonyan A, Kahr G, Rath T (2006) Determination of porosity and pore connectivity in feldspars from soils of granite and saprolite. *Soil Science*, **171**, 675–94.

Emmanuel S, Day-Stirrat RJ (2012) A framework for quantifying size dependent deformation of nano-scale pores in mudrocks. *Journal of Applied Geophysics*, **86**, 29–35.

Galaup S, Liu Y, Cerepi A (2012) New integrated 2D–3D physical method to evaluate the porosity and microstructure of carbonate and dolomite porous system. *Microporous and Mesoporous Materials*, **154**, 175–86.

Giesche H (2006) Mercury porosimetry: a general (practical) overview. *Particle & Particle Systems Characterization*, **23**, 9–19.

Hammes U, Frébourg G (2012) Haynesville and Bossier mudrocks: a facies and sequence stratigraphic investigation, East Texas and Louisiana, USA. *Marine and Petroleum Geology*, **31**, 8–26.

Hemes S, Desbois G, Urai JL, De Craen M, Honty M (2013) Variations in the morphology of porosity in the Boom Clay Formation: insights from 2D high resolution BIB-SEM imaging and Mercury injection Porosimetry. *Netherlands Journal of Geosciences*, **92**, 275–300.

Hildenbrand A, Urai JL (2003) Investigation of the morphology of pore space in mudstones—first results. *Marine and Petroleum Geology*, **20**, 1185–200.

Holzer L, Indutnyi F, Gasser PH, Münch B, Wegmann M (2004) Three-dimensional analysis of porous BaTiO3 ceramics using FIB nanotomography. *Journal of Microscopy*, **216**, 84–95.

Houben M (2013) In situ characterization of the microstructure and porosity of Opalinus Clay (Mont Terri Rock Laboratory, Switzerland). Fakultät für Georessourcen und Materialtechnik RWTH Aachen University, Dissertation, 192.

Houben ME, Desbois G, Urai JL (2013) Pore morphology and distribution in the Shaly facies of Opalinus Clay (Mont Terri, Switzerland): insights from representative 2D BIB–SEM investigations on mm to nm scale. *Applied Clay Science*, **71**, 82–97.

Houben ME, Desbois G, Urai JL (2014a) A comparative study of representative 2D microstructures in Shaly and Sandy facies of Opalinus Clay (Mont Terri, Switzerland) inferred form BIB-SEM and MIP methods. *Marine and Petroleum Geology*, **49**, 143–61.

Houben ME, Desbois G, Urai JL, de Winter DAM, Drury MR, Schwarz JO (2014b) Microstructure of the shaly facies of opalinus clay on the Mm-nm scale. In: *4th EAGE Shale Workshop Shales: What do they have in common?* pp. 36–40. EarthDoc, Porto, Portugal.

Hu Q, Ewing RP, Dultz S (2012) Low pore connectivity in natural rock. *Journal of Contaminant Hydrology*, **133**, 76–83.

Hu Q, Gao X, Gao Z, Ewing R, Dultz S, Kaufmann J (2014) Pore accessibility and connectivity of mineral and kerogen phases for shales. In: *Unconventional Resources Technology Conference*, Denver, Colorado, USA, URTeC-1922943.

Josh M, Esteban L, Delle Piane C, Sarout J, Dewhurst DN, Clennell MB (2012) Laboratory characterisation of shale properties. *Journal of Petroleum Science and Engineering*, **88–89**, 107–24.

Keller LM, Holzer L, Wepf R, Gasser P (2011) 3D geometry and topology of pore pathways in Opalinus clay: implications for mass transport. *Applied Clay Science*, **52**, 85–95.

Keller LM, Holzer L, Schuetz P, Gasser P (2013a) Pore space relevant for gas permeability in Opalinus clay: statistical analysis of homogeneity, percolation, and representative volume

element. *Journal of Geophysical Research: Solid Earth*, **118**, 2799–812.
Keller LM, Schuetz P, Erni R, Rossell MD, Lucas F, Gasser P, Holzer L (2013b) Characterization of multi-scale microstructural features in Opalinus Clay. *Microporous and Mesoporous Materials*, **170**, 83–94.
Klaver J, Desbois G, Urai JL, Littke R (2012) BIB-SEM study of the pore space morphology in early mature Posidonia Shale from the Hils area, Germany. *International Journal of Coal Geology*, **103**, 12–25.
Klaver J, Desbois G, Littke R, Urai JL (2015) BIB-SEM characterization of pore space morphology and distribution in postmature to overmature samples from the Haynesville and Bossier Shales. *Marine and Petroleum Geology*, **59**, 451–66.
Klinkenberg M, Kaufhold S, Dohrmann R, Siegesmund S (2009) Influence of carbonate microfabrics on the failure strength of claystones. *Engineering Geology*, **107**, 42–54.
Kuhn HA, Hughes WF, Gaylord EW (1962) Measurements of the viscosity of liquid Wood's Metal. *British Journal of Applied Physics*, **13**, 527.
Lloyd RR, Provis JL, Smeaton KJ, van Deventer JSJ (2009) Spatial distribution of pores in fly ash-based inorganic polymer gels visualised by Wood's Metal intrusion. *Microporous and Mesoporous Materials*, **126**, 32–9.
Mavko G, Mukerji T, Dvorkin J (2009) *The Rock Physics Handbook: Tools for Seismic Analysis of Porous Media*. Cambridge University Press, Cambridge.
Moro F, Böhni H (2002) Ink-bottle effect in mercury intrusion porosimetry of cement-based materials. *Journal of Colloid and Interface Science*, **246**, 135–49.
Nemati KM (2000) Preserving microstructure of concrete under load using the Wood's Metal technique. *International Journal of Rock Mechanics & Mining Sciences*, **37**, 133–42.
Nemati KM, Monteiro PJM (1997) A new method to observe three-dimensional fractures in concrete using liquid metal porosimetry technique. *Cement and Concrete Research*, **27**, 1333–41.
ONDRAF/NIRAS (2001) Safir 2 – Safety Assessment and Feasibility Interim Report 2. (Belgian agency for radioactive waste and enriched fissile materials) Brussels, Belgium.
Park YM, Ko D-S, Yi K-W, Petrov I, Kim Y-W (2007) Measurement and estimation of temperature rise in TEM sample during ion milling. *Ultramicroscopy*, **107**, 663–8.
Penumadu D, Dean J (2000) Compressibility effect in evaluating the pore-size distribution of kaolin clay using mercury intrusion porosimetry. *Canadian Geotechnical Journal*, **37**, 393–405.
Ross DJK, Bustin RM (2009) The importance of shale composition and pore structure upon gas storage potential of shale gas reservoirs. *Marine and Petroleum Geology*, **26**, 916–27.
Sigal RF (2009) A methodology for blank and conformance corrections for high pressure mercury porosimetry. *Measurement Science and Technology*, **20**, 12.
Terzaghi KV (1925) *Erdbaumechanik auf Bodenphysikalischer Grundlage*. Deuticke, Leipzig.
Thury M, Bossart P (1999) The mont terri rock laboratory, a new international research project in a mesozoic shale formation, in Switzerland. *Engineering Geology*, **52**, 347–59.
Urai JL, Nover G, Zwach C, Ondrak R, Schöner R, Krooss BM (2008) Transport processes. In: *Dynamics of Complex Intracontinental Basins* (eds Littke R, Bayer U, Gajewski D, Nelskamp S), pp. 367–88. Springer-Verlag, Berlin-Heidelberg.
Vandenberghe N (1978a) Sedimentology of the Boom Clay (Rupelian) in Belgium. Paleis der Academiën, Brussel.
Vandenberghe N (1978b) Sedimentology of the Boom Clay Formation (Belgium). *Bulletin van de Belgische Vereniging voor Geologie*, **102**, 5–77.
Viguier B, Mortensen A (2001) Heating of TEM specimens during ion milling. *Ultramicroscopy*, **87**, 123–33.
Washburn EW (1921) Note on a method of determining the distribution of pore sizes in a porous material. *Proceedings of the National Academy of Sciences*, **7**, 115–6.
Webb PA (2001) *An Introduction to the Physical Characterization of Materials by Mercury Intrusion Porosimetry with Emphasis on Reduction and Presentation of Experimental Data*. Micromeritics Instrument Corp., Norcross, Georgia.
Willis KL, Abell AB, Lange DA (1998) Image-based characterization of cement pore structure using Wood's Metal intrusion. *Cement and Concrete Research*, **28**, 1695–705.
Yadav GD, Dullien FAL, Chatzis I, Macdonald IF (1987) Microscopic distribution of wetting and nonwetting phases in sandstones during immiscible displacements. *SPE Reservoir Engineering*, **2**, 11.
Yang Y, Aplin AC (2007) Permeability and petrophysical properties of 30 natural mudstones. *Journal of Geophysical Research: Solid Earth*, **112**, B03206.
Yao Y, Liu D (2012) Comparison of low-field NMR and mercury intrusion porosimetry in characterizing pore size distributions of coals. *Fuel*, **95**, 152–8.
Zeelmaekers E (2011) Computerized qualitative and quantitative clay mineralogy: introduction and application to known geological cases. In: *Group Science, Engineering and Technology, Groep Wetenschap en Technologie: Heverlee* Leuven, Katholieke Universiteit Leuven, Dissertation, 397.
Zeszotarski JC, Chromik RR, Vinci RP, Messmer MC, Michels R, Larsen JW (2004) Imaging and mechanical property measurements of kerogen via nanoindentation. *Geochimica et Cosmochimica Acta*, **68**, 4113–9.

GEOFLUIDS

Volume 15, Number 4, November 2015
ISSN 1468-8115

CONTENTS

503 Palaeo-formation water evolution in the Latrobe aquifer, Gippsland Basin, south-eastern Australia continental shelf
J. Bourdet, R. Kempton and K. Michael

527 Fluid environment for preservation of pore spaces in a deep dolomite reservoir
D. Zhu, Q. Meng, Z. Jin and W. Hu

546 Boron isotope geochemistry of Na-bicarbonate, Na-chloride, and Ca-chloride waters from the Northern Apennine Foredeep basin: other pieces of the sedimentary basin puzzle
T. Boschetti, L. Toscani and E. Salvioli Mariani

563 Experimental investigation of carbon dioxide trapping due to capillary retention in saline aquifers
X. Li, M. Akbarabadi, Z.T. Karpyn, M. Piri and E. Bazilevskaya

577 The connectivity of pore space in mudstones: insights from high-pressure Wood's metal injection, BIB-SEM imaging, and mercury intrusion porosimetry
J. Klaver, S. Hemes, M. Houben, G. Desbois, Z. Radi and J.L. Urai

592 Multiphase flow simulation through porous media with explicitly resolved fractures
K. Su, J.-P. Latham, D. Pavlidis, J. Xiang, F. Fang, P. Mostaghimi, J.R. Percival, C.C. Pain and M.D. Jackson

608 Groundwater age, brine migration, and large-scale solute transport in the Alberta Basin, Canada
I. Gupta, A.M. Wilson and B.J. Rostron

WILEY
Blackwell

Geofluids* is abstracted/indexed in *Chemical Abstracts

This journal is available online at Wiley Online Library.
Visit onlinelibrary.wiley.com to search the articles and register for table of contents and e-mail alerts.